JOURNAL OF MATERIALS SCIENCE **34** (1999) 6045–6061

Sub critical crack advance vs. impact fracture on high impact polystyrene with different second phase volume contents and structures

C. MAESTRINI*, A. CALLAIOLI, L. CASTELLANI, A. FERRANDO
Enichem Research Centre, Via Taliercio 14, 46100 Mantova, Italy
E-mail: Claudio_Maestrini@HQ.enichem.geis.com

Also for polymers, many fractures in service occurs after a period in which an existing crack has propagated in a sub-critical manner, while the laboratory tests are mainly concentrated on impact fractures. Aim of this paper is then to investigate the sub critical fracture in some high impact polystyrene (HIPS) materials with different second phase volume fraction and particle size and to compare it with the outcomes of impact Fracture Mechanics experiments. Large differences in the results of the two mechanical test procedures are evidenced: the materials behaviour is then examined from the structural point of view and an interesting case of interfacial failure, which disappears at high strain rate, is attested on some HIPSs by means of different techniques, i.e. electron microscopy, nuclear magnetic resonance spectroscopy and dynamic mechanical spectroscopy, indicating that the slow crack fracture behaviour can be influenced by parameters that do not affect ordinary mechanical tests. © *1999 Kluwer Academic Publishers*

1. Introduction

Probably the majority of the catastrophic fractures that occurs in service for engineering parts develops after a period in which the crack has propagated in a *sub-critical* manner, i.e. in stress-strain conditions that cannot be considered critical if reproduced in short term experiments. This issue has now a great practical relevance also for polymers, due to the fact that they progressively tend to be used in more sophisticated applications: sub-critical fractures are, for example, an insidious problem in refrigerators, in which the failure of some polymeric part, whose cost is a very minor part of the total cost, can result in the rejection of the whole appliance [1].

A large amount of theoretical and experimental work has been dedicated to the sub-critical fracture (SCF) problem, the attention of the researchers being mainly focused on fatigue. An important basis of the work done has been the phenomenological law proposed by Paris and Erdogan [2, 3]: a cracked body is considered, the crack is assumed to be regular and planar, then well characterised simply by its length a, and the solicitations are supposed to be regularly cyclic, i.e. the load or the nominal strain are supposed to vary from a minimum value to a maximum value in a periodic way. Indicating with N the number of cycles, with da/dN the crack velocity, normalised over the period of the cycle and with K the stress intensity factor at the crack tip, a simple equation holds:

$$\frac{da}{dN} \cong A \cdot \Delta K^m, \qquad (1)^\dagger$$

where ΔK represents the variation between the maximum and the minimum stress intensity factors, $K_{\max}$ and $K_{\min}$, during a loading cycle, and A and m are constants which depend on the tests parameters and on the material's nature. Remarkable is the fact that the $K_{\max}$ in the Paris-Erdogan equation is generally well below the critical stress intensity factor, K_c, that the Irwin's criterion [5, 6] introduces for the corresponding material. The Paris equation holds also in case of monotonic solicitations if the crack speed replaces the crack advance over a cycle and the applied stress intensity factor the stress intensity factor variation over a cycle. This case is of course simpler than fatigue and free from side-phenomena like adiabatic heating: in the following, then, we will always consider it when we will talk about SCF.

On the other hand the everyday lab practice in industry tends to concentrate on impact fracture experiments (Izod, Charpy, etc.) in order to characterise the break-down behaviour of the materials: impact fracture

---

[*] Author to whom all correspondence should be addressed.

[†] In general the Paris-Erdogan law holds only for a limited range of values of ΔK, contained from a threshold value, ΔK_{th}, occuring when the crack-growth rate equals a value of approximately a few atomic distances per loading cycle, and a maximum value, ΔK_c, for which the crack-growth rate increases catastrophically. Furthermore, McEvily [4] has presented data, both his own and from the literature, that show that a well defined linear region of constant slope m (in a log-log plot of da/dN vs. ΔK) is not always found, giving a basis to the idea that the Paris-Erdogan behaviour is somewhat a limit condition or an approximation of a more complex law.

0022–2461 © *1999 Kluwer Academic Publishers*

experiments in fact are much more easy to perform, less time consuming and were considered up to the recent times strictly correlated to the real fractures occurring for polymeric parts. Also if the ordinary impact fracture tests have been largely criticised because of the dependence of their results on the tests conditions (see below), what cannot be denied is the fact that impact fractures continue to have an enormous practical relevance and that their characterisation is still extremely important in order to understand the material behaviour and to give to the customers necessary data for the applications.

Aim of this work is then to offer an example of comparison of the two fracture behaviours. The polymeric material that we have chosen to do that is high impact polystyrene (HIPS): HIPS is a polymeric substance composed of a main phase of polystyrene (PS) and of a second dispersed phase consisting of composite rubbery particles having an approximately spherical shape and various dimensions and structures. HIPS represents an interesting and relatively simple model system of the rubber toughening of brittle polymeric matrices [7]. PS in fact is extremely brittle: its tensile yielding mechanism is *crazing* (crazes differ from crack by the presence of many small polymer fibrils with diameter of about 6–9 nm and volume fraction of about 0.25, spanning from one craze-polymer interface to the other [8, 9]) and the increase in toughness (generally intended as the resistance to impact fracture) of HIPS with respect to PS is related to the effects of the rubbery particles on the crazing mechanisms, amply discussed on the literature on this subject (see for example reference [7]). Furthermore HIPS exhibits a very stable and easily observable SCF behaviour that can be readily modulated by changing the structural parameters (second phase volume fraction, size, structure, etc.).

It is clear then that in this case what one is interested in is the possible different role played by the rubbery second phase in the two different fracture conditions: in order to assess this role, the present work is completed by techniques other than SCF and impact testing, ranging form dynamic mechanical spectroscopy to electronic microscopy and nuclear magnetic resonance (NMR) spectroscopy.

2. Experimental

2.1. Materials

In the present paper we chose to analyse three different HIPSs, that we will indicate in the following with the letters from A to C, characterised by the presence of very diverse rubber particles with different dimension and structure (Figs 1–3).

Table I contains a summary of the molecular and structural parameters measured by means of common characterisation methods (described in the Table caption) for the considered materials. A PS homopolymer, indicated with the letter X, having molecular characteristics similar to those of the HIPS matrices is added to complete the data.

In order to realise a really precise and quantitatively useful structural characterisation, an accurate determination of the second phase volume fraction and of the particle size distribution is necessary. The ordinary way of measuring these two key parameters is, in fact, subjected to some criticism and gives rise to data that cannot be considered realistic [10]. For this reason, we adopted the stereological approach described in detail in the reference [10] and already tested in references [1, 11, 12] that consists in analysing transmission electron microscopy (TEM) pictures, obtained following the standard technique reported in the reference [13], from material slices having different thickness and then reconstructing the bulk situation. We used the following equations:

$$\langle r^1 \rangle = \frac{\pi \langle R^2 \rangle + 2t \langle R^1 \rangle}{4\langle R^1 \rangle + 2t}, \tag{2}$$

$$\langle r^2 \rangle = \frac{4\langle R^3 \rangle + 3t \langle R^2 \rangle}{6\langle R^1 \rangle + 3t}, \tag{3}$$

$$\phi_{\mathrm{app}} = \frac{4\langle R^3 \rangle + 3t \langle R^2 \rangle}{4\langle R^3 \rangle} \cdot \phi, \tag{4}$$

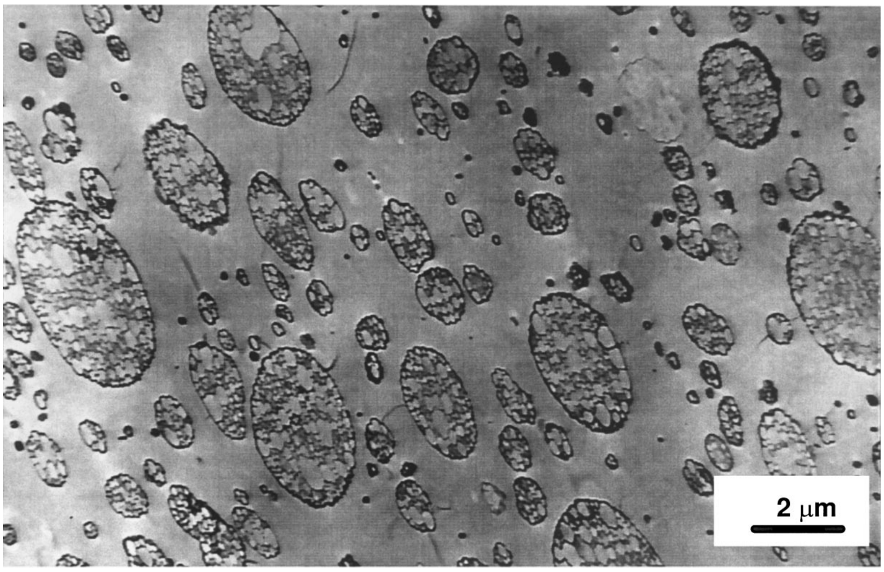

Figure 1 TEM micrograph of material A.

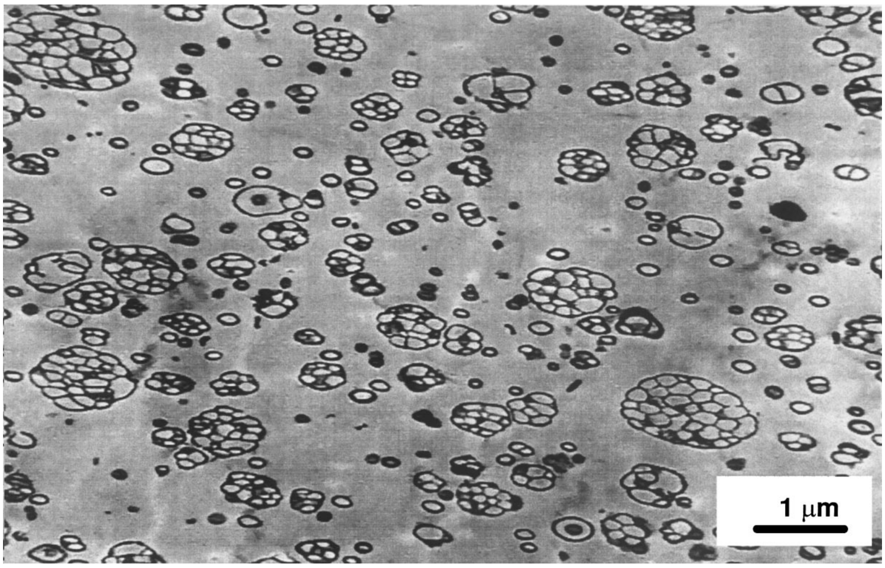

Figure 2 TEM micrograph of material B.

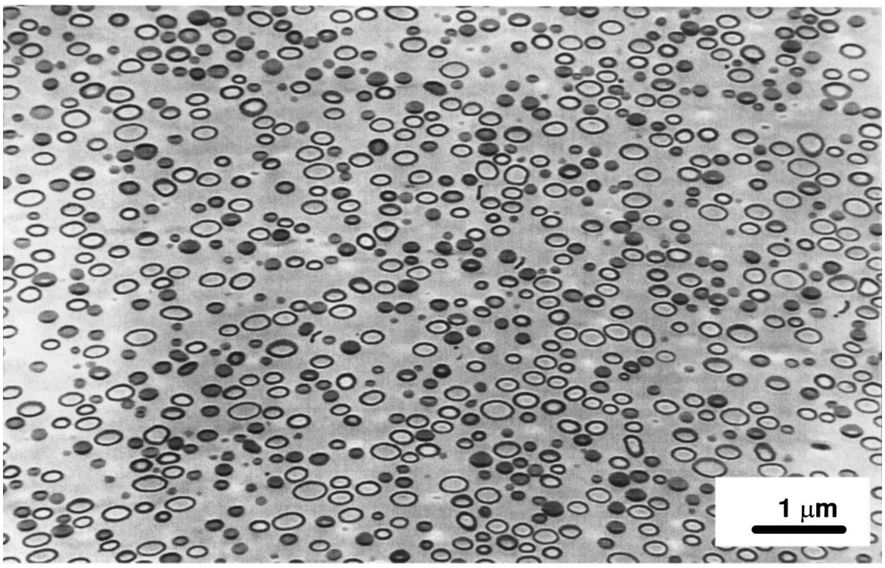

Figure 3 TEM micrograph of material C.

where the $\langle r^i \rangle$ represents the ith moment of the particle radius distribution in the TEM images, $\langle R^j \rangle$ the jth moment of the real particle distribution in the bulk, t the observed section thickness, ϕ_{app} the apparent second phase volume fraction in the TEM images and ϕ the real second phase volume fraction. The Equations 2–4, which produce an over-determined system when one considers more than one thickness, have been solved using a simple algorithm, which has been previously discussed in reference 12, and consists in the minimisation of the maximum component of a normalised linear error function containing all the parameters $\langle R^j \rangle$ and ϕ. Table I contains the outcomes of such a calculation.

Once the ϕ value was assessed on the materials, we produced, by melt mixing with PS X, some dilutions. In the rest of this paper the figure that follows the letter in the material indication refers to the percentage of ϕ for the considered dilution: e.g. A10 indicates the material A with a ϕ value of 10%.

2.2. SCF experiments

SCF experiments were performed in the following way: single edge notch (SEN) specimens, having width and thickness of approximately 45 mm and 6.4 mm, respectively were obtained from compression moulded plates. A preliminary saw-cut notch was introduced and then the samples were treated by sputtering on a side surface a thin gold grid (mesh size of about 1 mm), aimed to work as a dimensional reference. The samples were annealed at about 80 °C over night in order to achieve the same physical ageing conditions: this precaution is due to the fact that the SCF experiments take a relatively long time and that samples produced at the same time could be consequently tested in very different moments. Immediately before the mechanical tests, a razor notch, was tapped at the pre-notch tip with a fresh razor blade on each sample, and at that time each specimen was tested in tension (mode I fracture) on a ZWICK servo-hydraulic testing machine working under load control with a load rate of approximately 0.07 N/s, which was

TABLE I General parameters

	A	B	C	X
M_w	157 000	166 000	157 000	160 000
M_w/M_n	1.88	1.95	1.89	1.92
PB (%)	6.8	6.6	8.7	—
Particle struct.	Composite	Composite	Core-shell	
gel	0.26	0.22	0.28	—
Sw. index	13.6	13.5	13.8	—
ϕ	0.33	0.21	0.17	—
$\langle R^1 \rangle$	0.37	0.16	0.10	—

M_w: Weight average molecular weight of PS (g/mol) determined by gel permeation chromatography (GPC) with a refractive index detector on THF elution of the soluble part.

M_w/M_n: Polydispersity index of PS, measured as the ratio between the weight average molecular weight (M_w) and the average molecular weight (M_n) by GPC (see above);

PB: Weight fraction of PB (%) measured by titration methods and infrared spectroscopy.

gel: Second phase weight fraction measured by phase separation methods in selective solvent (the samples are dissolved and washed in MEK, the insoluble part is separated by centrifugation, precipitated by ethanol and then filtered, dried and weighted).

Sw. Index: Swelling index as weight ratio between swollen and dry *gel* (%). The dry gel is the one measured as in the above point, the swollen *gel* is weighted after 5 h from the centrifugation, but before the precipitation.

ϕ: Second phase volume fraction calculated from TEM pictures according to the stereological approach described in reference [10] and summarised in the Equations 2–4 of the present paper.

$\langle R^1 \rangle$: First moment of the particle radius distribution (number average particle radius) in μm calculated from TEM pictures according to the stereological approach described in reference [10] and summarised in the Equations 2–4 of the present paper.

the same for all the materials. At least three convincing samples were tested for each material.

A camera with magnifying objective lenses of about 30× was used in order to follow the fracture advance: such a magnification was sufficient to have a good resolution of the crack tip position. The camera was mounted on a positioner device that allowed very small displacements, keeping the images still during the motion. Thus, the images were recorded on a VCR and synchronised to the load cell signal by means of a frame code generator. The frames were successively printed by means of a video printer and the values of the fracture coordinate were simply obtained from the pictures: it was, at that moment, possible to get sets of data, relative to the position of the fracture on the side surface of the sample and to the applied load at the same instant for each fracture.

The K value at a given instant t was given by the formula [14]:

$$K(t) = \frac{Y \cdot P(t)}{B \cdot W}\sqrt{a(t)}, \tag{5}$$

where $a(t)$ is the crack coordinate, $P(t)$ was the applied load at the same time t, W and B the specimen width and thickness, respectively, and Y is a form factor given by [15]:

$$Y = 2.0113 + 0.1763 \cdot \frac{a}{W} + 3.9365 \cdot \left(\frac{a}{W}\right)^2 - 8.1733 \cdot \left(\frac{a}{W}\right)^3 + 8.3378 \cdot \left(\frac{a}{W}\right)^4. \tag{6}$$

The Equations 5 and 6 hold when $0.2 < a/W < 0.8$: data out of this range were never considered.

For the determination of the crack speed we adopted the following method: in the reference [1] we observed that the plot of the measured $a(t)$ values vs. $\log(1/(t_f - t))$, where t_f is the total fracture time, were well approximated by straight lines. In order to improve the data fit we assumed here that:

$$a(t) = \sum_{i=0}^{4} \alpha_i \cdot \left[\log\left(\frac{1}{t_f - t}\right)\right]^i, \tag{7}$$

and computed the α_i from the experimental data. Of course the value of da/dt can be easily extracted from the Equation 7 by a simple time derivative operation. At this point, then, Paris plots of $da(t)/dt$ vs. $K(t)$ are easily attainable for each sample.

2.3. Fracture mechanics measurements on impact tests

Ordinary impact tests on notched specimens are conducted according to standardised norms (ISO, ASTM, DIN, etc.) for Charpy or Izod pendula and the quantity which is determined is the total energy to fracture. These tests, however, have been criticised for several reasons, which can be summarised simply saying that the outcome of these measurements are not intrinsic material characteristics, depending instead on the test conditions. Nonetheless, several attempts have been made in order to apply the Fracture Mechanics approach to this kind of measurements. The one that has proved to fit well to our case is also the simplest one: it can easily be described as follows [16].

In a generic ductile material it holds:

$$U - U_k = B \cdot (W - a) \cdot G_c, \tag{8}$$

where U is the total energy absorbed by the specimen during the fracture process, U_k is the specimen kinetic energy, G_c is the critical energy release rate and B, W and a are the specimen thickness, width and the crack length, respectively. If specimens having different initial crack lengths are prepared and tested, all parameters in the Equation 8 can be measured, with the only exception of G_c, which has proved to be an intrinsic parameter and that can be thus extracted as the slope of a plot of $U - U_k$ vs. $B \cdot (W - a)$.

In order to obtain similar plots for the materials considered in the present work, compression moulded specimen, having the following dimensions: 60 × 12.8 × 6.4 mm, were prepared. The size and specially the thickness have been chosen according to the experimental set-up features (thicker samples were not easily suitable): then the requirements for plane strain fracture were not necessarily satisfied. A razor notch after a machine notch was introduced, having different initial depth in each sample (the measure of the initial crack length, corresponding to the razor notch depth, was obtained by means of optical microscopy on the fractured samples). The fracture experiments were performed on an instrumented pendulum with a hammer

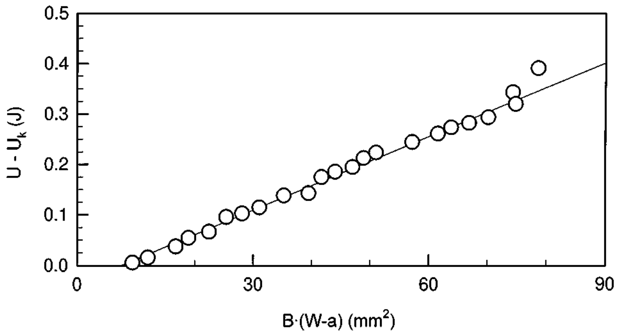

Figure 4 Plot of $U - U_k$ vs. $B \cdot (W - a)$ for material A20. The line represents a regression (the last two point have been excluded).

of 4.195 kg using supports with ratio $L/W = 4$, where L is the support span. The speed of the hammer at the impact was of 2 m/s, while the nominal strain rate of approximately 60 s^{-1}. The kinetic energy of the specimen was simply determined by measuring the throw energy of the specimen in absence of supports as a function of the specimen weight.

Fig. 4 is a plot of $U - U_k$ vs. $B \cdot (W - a)$ for material A20, which is nonetheless representative also of the case of all other tested materials. The plot is linear confirming the substantial validity of Equation 8. The fact that the plot shows a negative intercept, already noticed in the literature [14, 17], has been explained by the fact that low values of $B \cdot (W - a)$ correspond to conditions in which the plastic zone cannot fully develop. In some cases a positive deviation from the linearity was observable in correspondence of high values of $B \cdot (W - a)$ and these data were not considered for the determination of the energy release rate. G_c values were obtained from linear regressions from plots like the one in Fig. 4, simply as the slope of the linear trend.

2.4. Other experimental techniques

2.4.1. Elastic and plastic properties

Table II contains the experimental data for the shear modulus, μ, and the Young modulus, E, for the HIPS considered materials: E and μ were measured on compression moulded specimens adopting a three-point bending and a simple torsion geometry, respectively, both in dynamic regime with sinusoidal strain pulses at a frequency of 1 Hz with the maximum strain achievable in the linear viscoelastic zone.

In Table II the values of the yielding stresses for the considered materials are also reported: the yielding experiments were performed in tension on compression moulded specimens having dimensions: 45 mm (gauge length) × 10 × 2 mm, at a nominal strain rate of $4 \cdot 10^{-4}$ s^{-1}. The yielding point, σ_y, was considered as the average on at least five measurements of the maximum in the stress-strain curve.

2.4.2. Dynamic mechanical measurements

Dynamic mechanical analysis of materials A and B was carried out on compression moulded specimens (size: $12 \times 2 \times 55$ mm) in three point bending, with imposed sinusoidal strain (maximum strain = 0.03%) at a frequency of 1 Hz. Test temperature ranged from $-150\,^{\circ}$C to matrix T_g (about $100\,^{\circ}$C), with a scan rate of $1\,^{\circ}$C/min.

TABLE II Elastic and plastic parameters

	E	μ	σ_y
A30	1560	660	12.8
A20	2160	830	15.1
A10	2650	1090	19.0
A5	3050	1230	22.5
B20	2060	850	22.7
B10	2635	1100	26.4
B5	3050	1235	23.5
C17	2025	790	20.2
C10	2395	980	21.9
C5	2885	1150	23.2

E: Young modulus (MPa). The experimental procedure is described in the text.

μ: Shear modulus (MPa). The experimental procedure is described in the text.

σ_y: Yield stress (MPa). The experimental procedure is described in the text.

2.4.3. Examination of the microscopic plastic deformation features

Microtomed polymer slices of the materials under investigation can be easily bonded to treated copper grids by means of simple temperature cycles above T_g, as outlined in the reference [23], strained after annealing over night at about $80\,^{\circ}$C and observed by transmission electron microscopy (TEM) in a way perfectly similar to that described by Lauterwasser and Kramer [18]. We adopted two different straining procedure, the first one, taking advantage of the almost perfect plasticity of annealed copper, was realised outside the microscope, by deforming the grids on a motorised microdynamometer with a strain rate of approximately 10^{-4} s^{-1}, up to the maximum deformation reachable before fracture (2–3%), grid regions were then cut and put in the TEM (100 KeV) chamber for the observation. The second procedure consisted in the utilisation of a PHILIPS straining device integrated in the TEM sample holder (in this case very light copper grid have to be used to allow deformation inside the specimen holder), the achievable strain rate ranged approximately from 10^{-4}–10^{-2} s^{-1}. Crazes have been photographed in conditions of slight under-focus and under-exposure, in order to enhance the visual quality of the images.

2.4.4. Examination of the fracture surfaces

Fractured samples from SCF and impact experiments were observed for A and B materials, after the sputtering of a gold thin layer, by means of a scanning electron microscope (SEM) ZEISS DSM 960 (30 KeV), according to standard procedures.

2.4.5. NMR characterisation

As it will be clear in the following, some of the investigated materials appear different in terms of PS-PB interfacial features. A new and stimulating way to investigate the interfacial properties is given by the solid state NMR technique. For this reason spectra for some of the considered materials (A20, A30, B20) were collected at room temperature on a BRUKER AC-300P spectrometer at field of 7.05 T in a BRUKER multinuclear X/^{1}H dual-channel probehead for CP/MAS experiments. The spinning rate was 4850 Hz, that allowed to have spinning side bands outside the polymer signals. Every spectrum was constituted by 128 experiments of 1024 scans with a dwell time of 5 μs for each one. Cross polarisation contact time was 1 ms. The Wideline Separation (WISE) 2D sequence without ^{1}H spin diffusion was used as described by Schmidt-Rohr *et al.* [19] in order to elucidate the data.

3. Results and discussion

Figures from 5–7 contain the Paris plots for the considered materials: it is immediate to observe that the SCF behaviour is extremely different in different materials but that in all cases there is at least a region in the plot that fits well the Paris law (Equation 1). The case of material B—mainly B5—is complicated by the phenomenon of discontinuous crack growth (crack jumping). It is evident here that the particles size and structure play a relevant role, but, quite surprisingly, the second phase volume fraction appears from a first analysis of the Paris plots to have a detrimental effect: in fact, in correspondence of the same applied stress intensity factor, the fracture velocity is higher when the second phase volume fraction is higher.

On the other hand, Fig. 8 is a plot of the G_c values for the considered materials: from this plot it is evident and remarkable that in this case no appreciable difference exists among the materials and that ϕ seems to be the only parameters affecting the impact toughness (at least in the examined ϕ range)[‡]. As expected from what is known on the toughening, the fracture resistance is greater when the second phase volume fraction is higher.

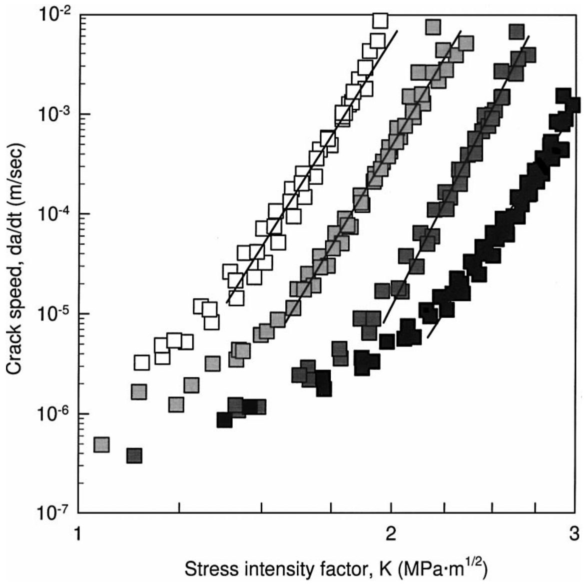

Figure 5 Paris plot for material A. Data from left to right are relative to materials: A30 (empty squares), A20 (light grey squares), A10 (dark grey squares) and A5 (black squares), respectively. The lines are guides for the eye that evidence the regions of Paris regime (Equation 1 in the text).

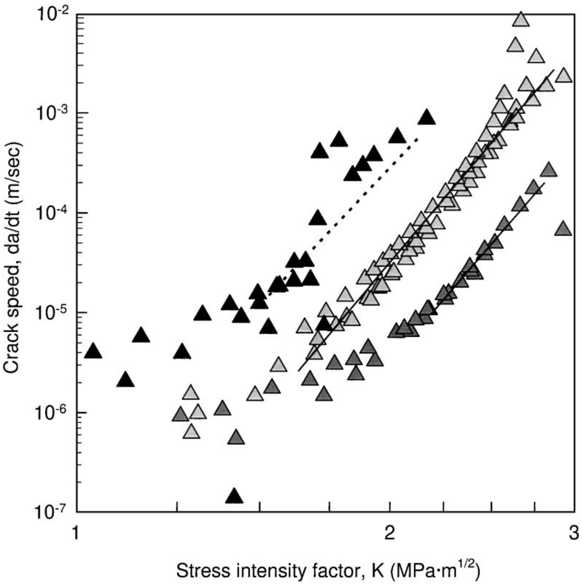

Figure 6 Paris plote for material B. Data are relative to materials: B20 (light grey triangles), B10 (dark grey triangles) and B5 (black triangles), respectively. The lines are guides for the eye that evidence the regions of Paris regime (Equation 1 in the text); the line relative to material B5 is dotted due to the fact that in this case very frequent crack jumping was observed.

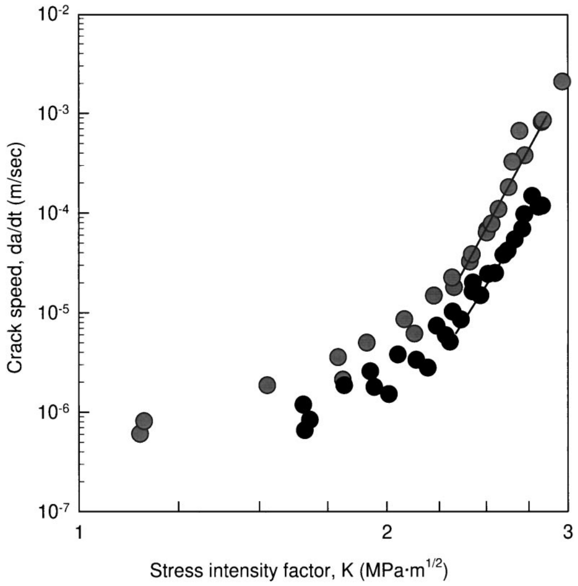

Figure 7 Paris plot for material C. Data are relative to materials: C10 (dark grey circles) and C5 (black circles), respectively. The lines are guides for the eye that evidence the regions of Paris regime (Equation 1 in the text).

The discrepancy between the two different fracture tests requires an explanation: it is in fact quite hard to merely imagine that the effect of the particles could be

[‡] From the data examination it is possible to imagine that in correspondence to high values of the second phase volume fraction the toughness of material C will increase less than in the case of salami HIPS. Unfortunately we do not have access to experimental data that can confirm this hypothesis because materials like C cannot be easily produced having higher second phase volume content.

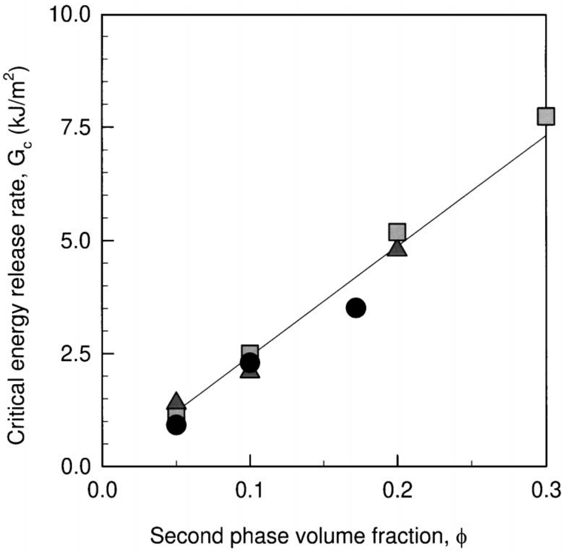

Figure 8 Plot of the criticle energy release rate G_c, vs. the second phase volume fraction, ϕ. Squares are relative to material A, triangles to B and circles to C. The line is a regression on all the data.

positive on impact tests and negative on slow fracture experiments.

A possible solution comes from the recognition that Fig. 8 and Paris plots contain different informations. If we want to understand the SCF behaviour in microscopic terms we have then to remember that in a material like HIPS, containing a dispersed phase, besides the stress intensification due to the crack itself, another distortion of the stress field is present, originated from the mismatch in the elastic constants between the matrix and the second phase. The stress intensification due to the rubbery particle is in fact the basis of the toughening mechanism, being the reason of the multiple crazing nucleation [7]. In order to have an idea of the real stress distribution in HIPS, it could be then very interesting to try to estimate a value of the stress intensity factor referred to the matrix, taking into account also the stress concentration effect due to the rubbery particles.

The calculation of the stress concentration around a single particle has been obtained in a mathematical way by Goodier in a classic paper [20]. This calculation however cannot be applied to real cases: in substance the Goodier model appears too schematic because evidence exists that the second phase stress concentration depends both on the particle size and concentration [11]. Nonetheless we can use an indirect way to estimate the concentration capability of the rubbery particles: if we assume that the matrix crazing stress stays unchanged, the reduction with respect to this value manifested by the HIPS yield stress in tensile tests should provide a reliable measure of the stress concentration ability of the particles: we can then estimate for each material an intensification factor due to the presence of the second phase, f, defined as:

$$f = \frac{\sigma_c}{\sigma_y}, \tag{9}$$

where σ_y is the yield stress and σ_c the matrix crazing stress, and then assume that the stress intensity factor on the matrix, K_m, could be given by:

$$K_m = f \cdot K. \tag{10}$$

The Paris plots can be now constructed in terms of K_m instead of K.

This has been done in Fig. 9 (where a matrix crazing stress of 25 MPa was assumed according to Kramer [8]): from the analysis of the figure it is evident that the behaviour of materials A and C (squares and circles) becomes now comprehensible: the effect of the rubbery particle size and concentration is simply accounted by the stress concentration factor: approximately in fact the same stress intensity factor on the matrix produces the same crack speed. Using this approach we can arrive, then, to a congruency with the impact fracture behaviour: in fact if the fracture is governed by the stress on the matrix, it is clear that materials containing more dispersed phase, which can henceforth develop more efficiently plastically yielded zones, dissipates more energy, as in fact it is illustrated in Fig. 8.

Different is the situation for material B, which in Fig. 9 appears more *fragile* (triangles), having crack speed values much higher if compared with the other ones in correspondence of the same stress intensity factor on the matrix. It has to be said here that this plot captures well the *fragility feeling* that we had during the SCF experiments on the B materials, enhanced also by the presence of the discontinuous crack growth phenomenon (crack jumping). For this reason, the Fig. 9 evidences to our opinion a real difference that exists between the impact fracture and the SCF behaviour of B: in the first case (impact) B is as tough as its counterparts with the same amount of dispersed phase, while in the second case (SCF) it appears remarkably more brittle.

We will come back later on this difference between impact and slow fracture behaviour, yet let us concentrate for the moment on the fragility of B in SCF experiments. In order to understand it, it is useful to examine more in detail the yielding behaviour of the considered

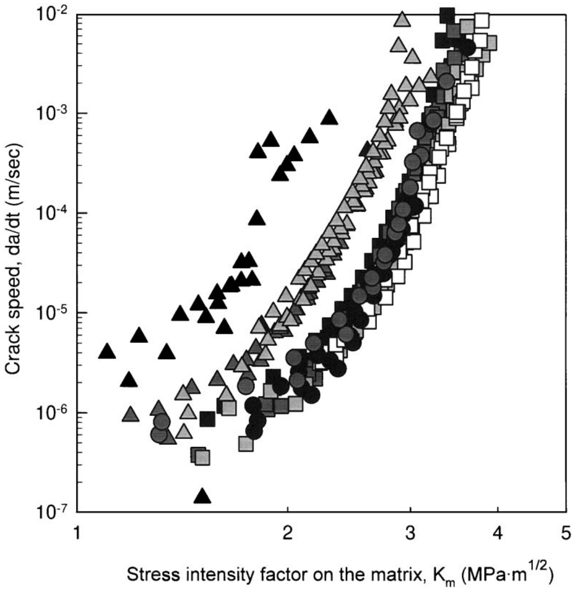

Figure 9 Plot of the crack speed, da/dt vs. the stress intensity factor on the matrix, K_m. The symbols are connected to the considered materials as follows: black squares: A5; dark grey squares: A10, light grey squares: A20; empty squares: A30; dark grey triangles: B10; light grey triangles: B20; black circles: C5; dark grey circles: C10.

materials. We recently found, in a study dedicated to core- shell HIPS [21], that the yield stress is easily derived from the equation:

$$\sigma_y = \sigma_c \cdot (1 - \phi). \tag{11}$$

The equation is a simple modification of the well known Ishai and Cohen equation [22]:

$$\sigma_y = \sigma_0 \cdot \left(1 - \sqrt[3]{\frac{9\pi}{16} \cdot \phi^2}\right), \tag{12}$$

in which the specimen effective section is computed, instead that in the hypothesis of a particle cubic lattice arrangement (Equation 12), assuming a more realistic random distribution and referring to the stereological Delesse-Rosiwal principle (Equation 11) [10].

Fig. 10 is a plot of the normalised yield stress, in which both the Ishai-Cohen and Delesse-Rosiwal normalisations are considered vs. ϕ for C and some comparable other materials that we investigated in a previous papers of ours (see Figure captions for details): straight horizontal lines in this kind of plot mean that the relative normalisation works well, lines or curves which are not horizontal mean that the yield behaviour cannot be simply understood in term of a reduction of the specimen cross-section. Fig. 10 plainly confirms, then, that for core-shell HIPSs the Equation 11 is a good description of the yield phenomenon.

On the other hand, Fig. 11 depicts a different situation: the yield stress of large salami HIPS (materials A and B in the present work and materials from reference 10) cannot be corrected by the Delesse-Rosiwal normalisation.

In the case of A one obtains a line with slope definitely negative. This situation, however, is at least qualitatively comprehensible: in materials like material A the stress intensification due to the particles cannot be neglected and it has to be added to the cross section reduction. Thus fact that the Delesse-Rosiwal normalisation produces a negative slope plot indicates that the factual stress intensification due to the particles increases with increasing the second phase content.

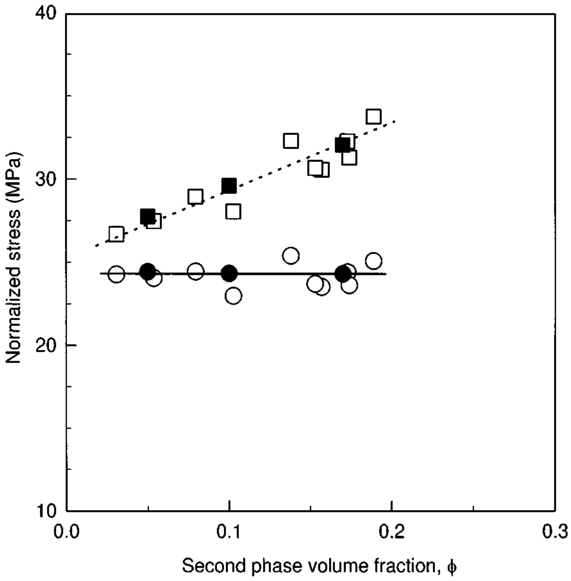

Figure 10 Plot of the normalised stress at yield vs. the second phase volume fraction ϕ, for core-shell HIPS materials: squares are relative to the stress normalisation according to the Ishai and Cohen formula (Equation 12 in the text); circles to the stress normalisation according to the Delesse and Rosiwal stereological principle (Equation 11 in the text); filled symbols are for material C considered in the present paper, empty symbols are from references [10] and [21]. The solid and dashed lines are simply guides for the eye.

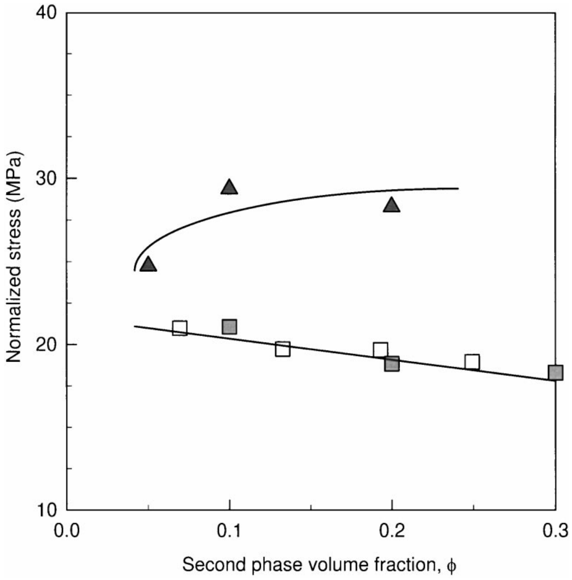

Figure 11 Plot of the normalised stress at yield vs. the second phase volume fraction, ϕ, for composite (salami) particle HIPS materials: the considered stress normalisation is according to the Delesse and Rosiwal stereological principle (Equation 11 in the text); grey squares and triangles are for material A and B, respectively, considered in the present paper, empty squares are from reference [10]. The solid line and curve are simply guides for the eye.

What we observe instead for B is the very reason of its anomalous behaviour in the Paris plots vs. K_m (as it is clear from the mathematical definition of this last parameter). We do not consider really relevant the dependence of the yield stress on the second phase volume fraction for this material because of some scatter in the data, nonetheless what in our opinion is significant is the fact that the yield stress is very high (Table II), close to values that can be assimilated to the crazing stress of the matrix. This means that the rubbery phase capability to produce and stabilise multiple crazes, which is the very reason of yield stresses lower than the crazing of the matrix, is extremely poor in B, even poorer than in the case of C.

If in the case of materials like C the explanation for high yield stress values has already be found in the fact that small particles cannot efficiently nucleate the crazes [23], the same way of reasoning is hard to sustain for B: particles in B, in fact, have a size and a structure such that craze nucleation should be enhanced as in the case of material A[§].

[§] It has to be noticed here that, as far as the elastic properties of the materials are concerned, no relevant anomaly is evident. In a previous paper we demonstrated that, knowing the structural characteristics of the second phase, it is possible to compute on the basis of a solid model, the elastic properties of the whole materials [11]. The materials considered here are no exception to this principle: they in fact have been used (and are easily recognizable), together with others, in order to test the model in the very same reference [11].

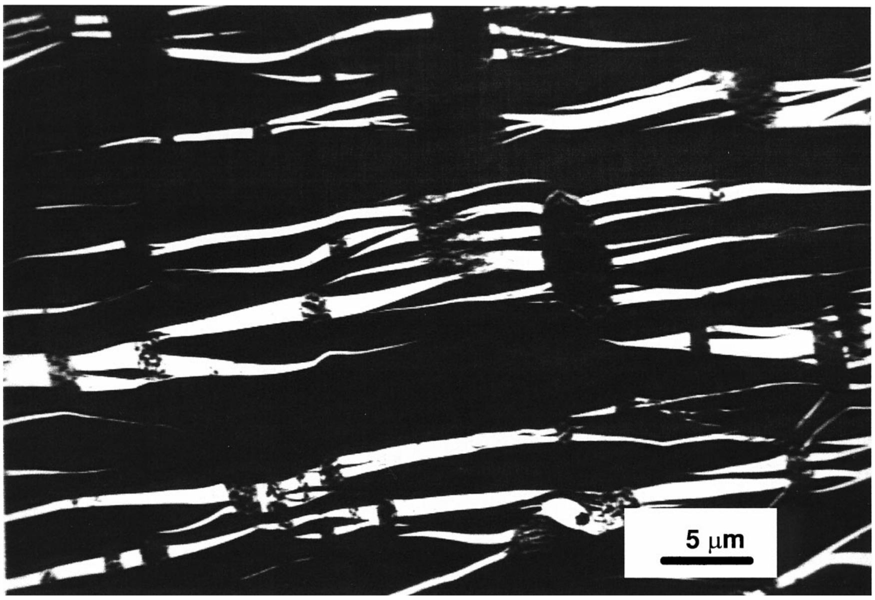

Figure 12 TEM picture of crazes in material A5. Multiple crazes nucleated and stopped at the particle-matrix interface are clearly visible.

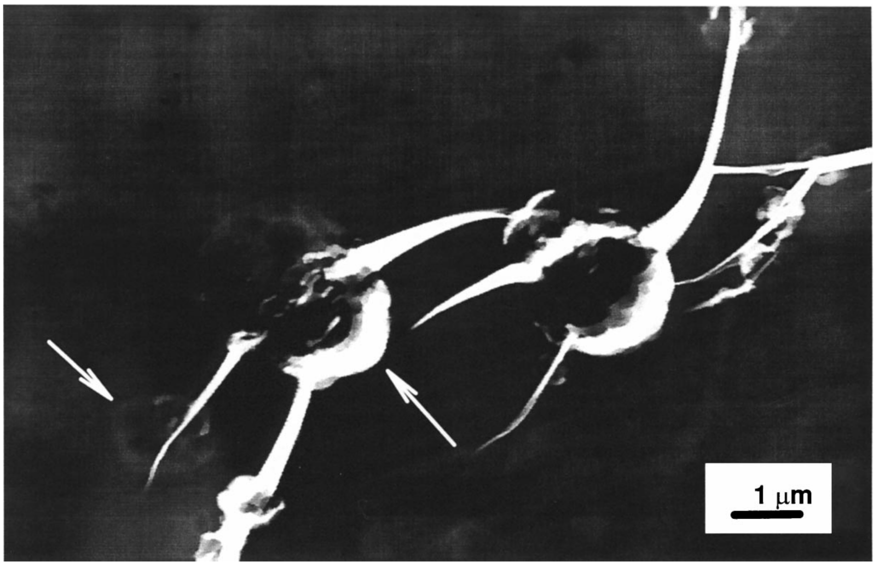

Figure 13 TEM picture of the plastic deformation in material B5: the two arrows evidence the failed craze stopping and the subsequent particle breakdown (left)and the particle-matrix failure (right).

A possible solution to this problem can be found by means of the TEM investigation of the plastic deformation mechanisms. Figures from 12–14 are pictures of plastically deformed zones for materials from A to C. In the case of the first and last materials (A and C) nothing unusual is visible: large salami particles nucleate and stop the crazes, which form in dense bundles (Fig. 12), while small core shell particles are trapped inside the crazes (Fig. 14). Both mechanisms have been already observed and discussed in the literature. Furthermore, the micromechanics of the plastic deformation is congruent with the different yield behaviour in the two materials, confirming the fact that in material A the particles provide an appreciable source of stress intensification, while in C they do not.

For material B the situation is different: the particles do nucleate crazes but they appear not good in stopping them (a particle cut by a craze is visible and put in evidence in the Fig. 13), moreover debonding of the particles is also visible. This situation is really general: it has been observed in wide regions of the deformed specimens without significant limitations in the strain rate range applicable with the TEM straining sample holder. Furthermore the use of this tool cancelled the doubts about the possible production of the interface failure during the cutting process during the specimen preparation: the interface debonding was in fact directly observed to occur during the deformation.

Clearly craze bundles cannot easily develop in this material: when crazes propagate they do not find obstacle in the particles, having a higher probability to degenerate into catastrophic cracks. The situation is made even worse by the fact that the particle-matrix interface fails providing crack nuclei inside the material. In other words, material B is brittle in SCF experiments simply because the damage induced by the particles prevents the mature development of the crazes. This microscopic evidence explains at least qualitatively the yield stress

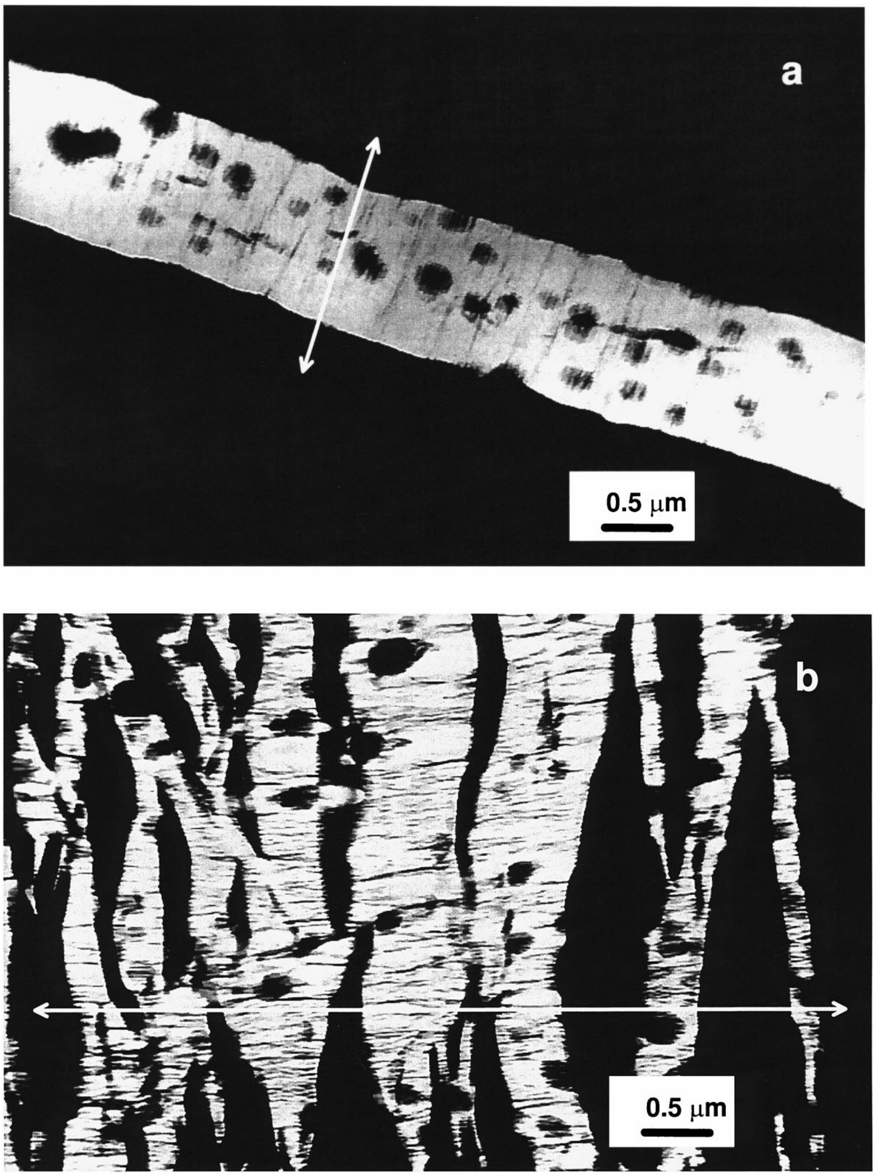

Figure 14 (a) TEM picture of the plastic deformation in material C5; and (b) in material C10. The white arrows indicate the strain directions.

behaviour for B and then also its anomaly in the Paris plots vs. the stress intensity factor on the matrix.

We can at this point try to understand the micromechanical behaviour of B in terms of its structural features. Let us consider first the particle-matrix debonding phenomenon. In order to do that it is useful here to introduce and discuss the results of the dynamic mechanical measurements. Figs 15 and 16 contain the plot of tan δ vs. temperature for A and B, respectively, in a region in which the PB glass transition is visible. Taking into account that all materials contain PB with exactly the same isomeric composition, no appreciable T_g shift should be observable. However this is not the case for our materials, as shown in Fig. 17 in which the PB T_g values (computed ad the abscissas of the tan δ peaks) are plotted vs. ϕ.

In order to explain this situation we propose the following idea: due to the thermal expansion mismatch between PS and PB, thermal stress can arise in two phases materials [24]. Thermal stresses have been calculated by Pavan and Riccò [25] for a model system in which a composite particle containing a spherical

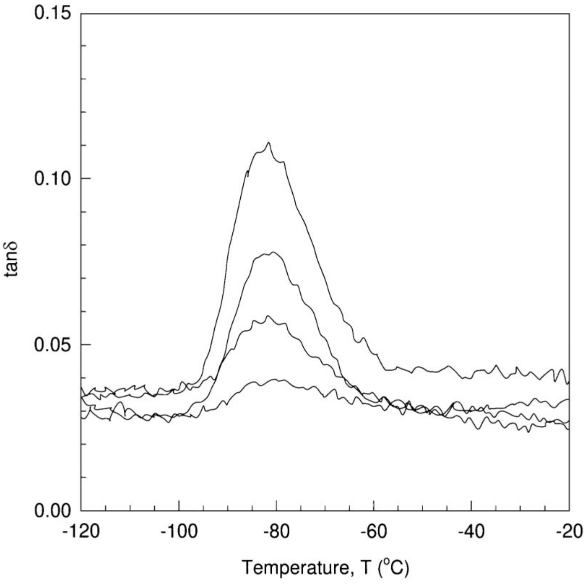

Figure 15 Plot of tan δ vs. the temperature, T, for material A. The curves correspond to A5, A10, A20 and A30, going from the lowest to the highest.

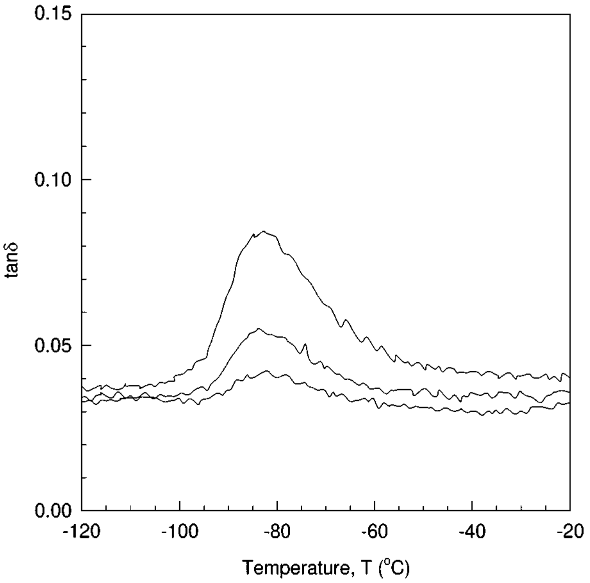

Figure 16 Plot of tan δ vs. the temperature, T, for material B. The curves correspond to B5, B10 and B20, going from the lowest to the highest.

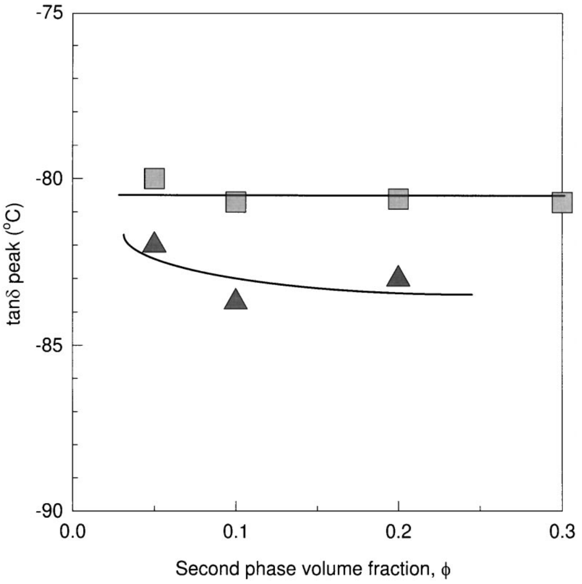

Figure 17 Plot of the temperature at which tan δ has a peak corresponding to the PB T_g vs. the second phase volume fraction, ϕ, for materials A (light grey squares) and B (dark grey triangles). The lines are simply guides for the eye.

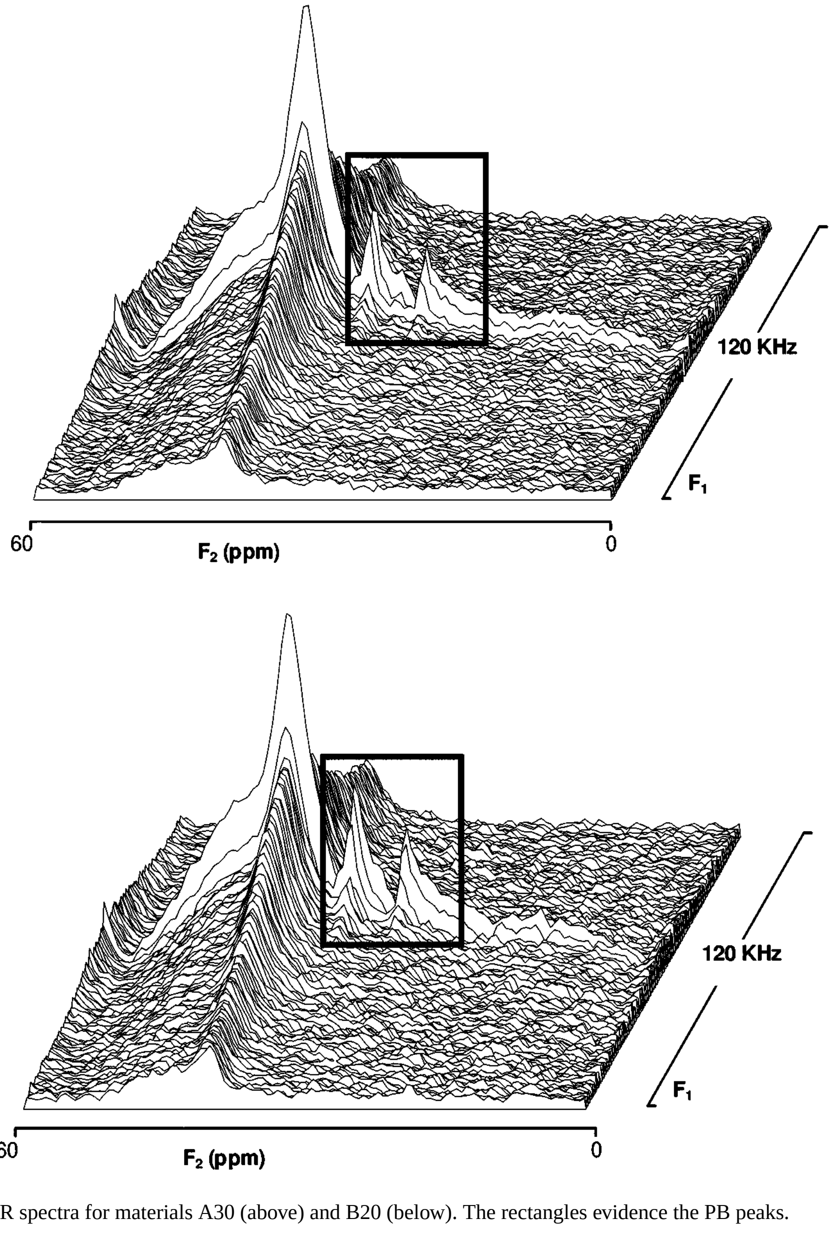

Figure 18 WISE 2D NMR spectra for materials A30 (above) and B20 (below). The rectangles evidence the PB peaks.

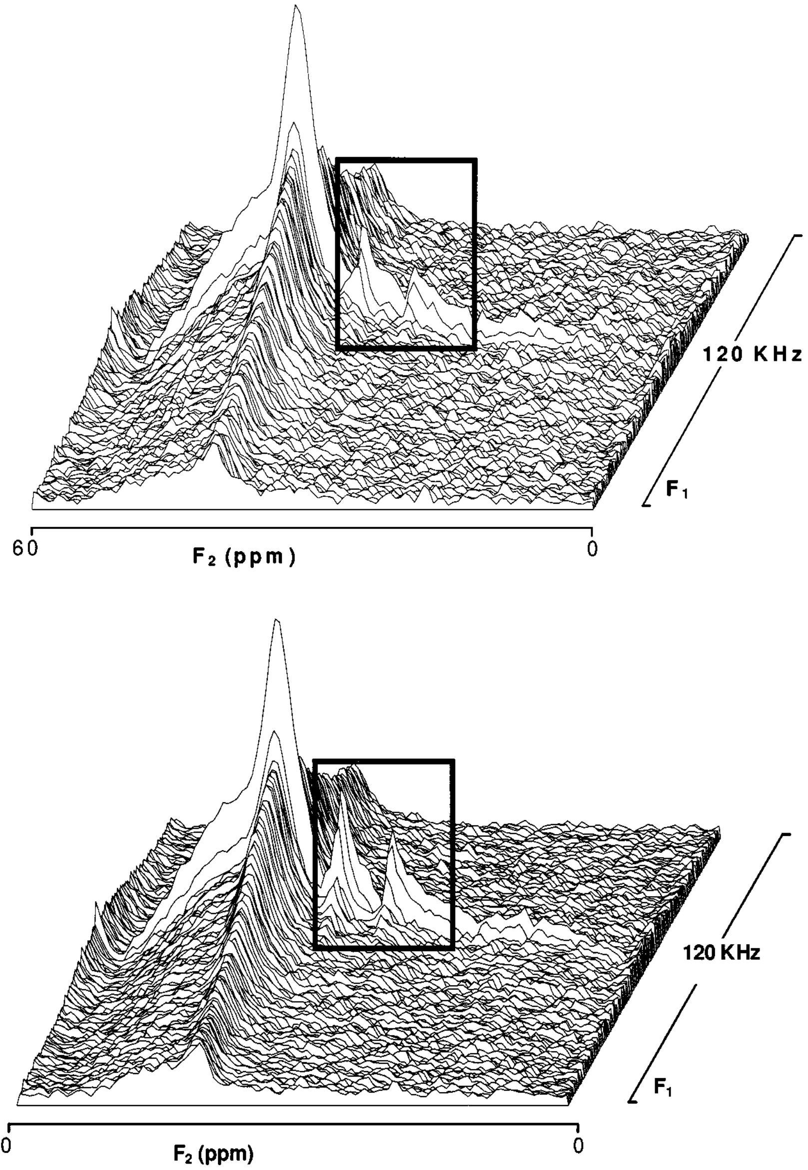

Figure 19 WISE 2D NMR spectra for materials A20 (above) and B20 (below). The rectangles evidence the PB peaks.

rigid sub-inclusion is surrounded by a rigid matrix. It was shown that the thermal stress, which is maximum for a pure rubbery particle with no sub-inclusions, is strongly decreased as the amount of the rigid component increases inside the particles. A qualitative indication of the degree of rigid (PS) sub-inclusion for the HIPS particles can be given by the ratio between ϕ and the rubber content (Table I): this gives values of about 5 and 3 for materials A and B, respectively. The degree of thermal stress then should be higher in B than in A¶. And the existence of a difference in the two materials also regarding this issue is confirmed by the Fig. 17, in which the PB T_g results in fact lower for B than for A.

However it is easy to demonstrate that the thermal stress is higher when the second phase content is lower, while we observe that the PB T_g difference between the two materials tend to disappear in correspondence of low ϕ values. This apparent contradiction can nonetheless be explained if we take into account the PS-PB interface debonding evidenced in Fig. 13: it has already been observed that the thermal stress can reach values for which cavitation or interfacial failure of the particle manifest [12]. We can assume then that the thermal

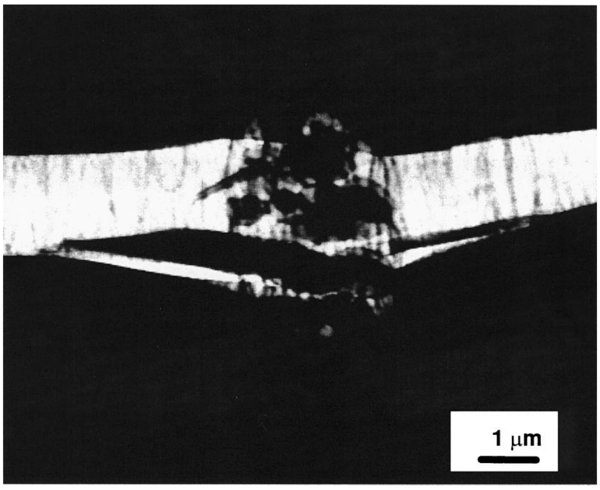

Figure 20 TEM picture representing the intra-particle craze fibrillation in material A.

¶For materials with particles with the same degree of sub-inclusion of A, it has been demonstrated that the thermal stress is almost absent [12].

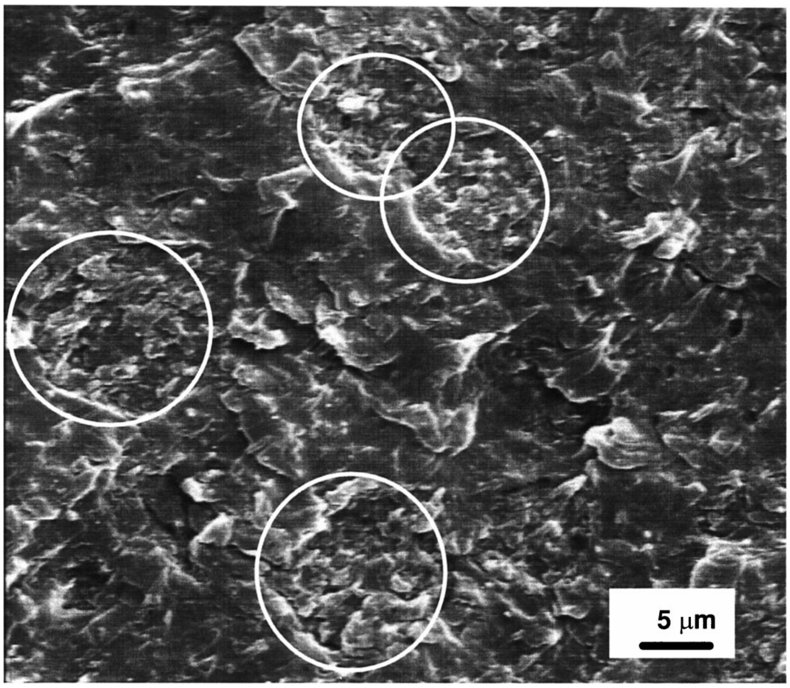

Figure 21 SEM micrograph of a SCF surface in material A20. Circles evidence bonded, broken particles.

stress values in B materials with low ϕ could be sufficient to produce some interface failure, with the subsequent release of the stress and the alignment of the PB T_g values to those for A. If this is true, interface debonding in material B is indirectly confirmed also by dynamic mechanical experiments. We have now to try to explain its origin.

Up to now it has ordinarily been assumed that, because of the polymerisation reaction involved [7], the quantity of the interfacial matter in HIPS (PS-PB graft copolymer) is high and then sufficient to grant a good adhesion between the matrix and the rubbery particles. Furthermore, at a first sight one could also conclude that, because of the fact that particles in B are smaller than in A, B should posses an equally efficient (or even better) interface between matrix and second phase. The only particle size, however, is not a good indicator of the interfacial properties in HIPS, being governed by factors other than the interfacial tension, namely the shear stress during the polymerisation process and the viscosity ratio between the phases [7]. In addiction the quantity of interfacial matter alone, which can efficiently reduce the particle size, can in principle be not directly related to the mechanical adhesion. Molecular weight of branches in the graft copolymers, for example, is likely to play a key role on the mechanical characteristics of the interface [26, 27].

Thus it would be necessary at this point to obtain direct information on the interfacial properties in A and B materials. Nevertheless, to accurately characterise the PS-PB interfacial matter in HIPS and to refer its features to the mechanical adhesion properties is not an easy task. Recently NMR spectroscopy has been applied in a way that can be useful here [28]. WISE 2D spectra have in fact been used to investigate the micromorphology and interface properties of polymeric materials, especially of blends or copolymers that have a soft and a hard phase. In these cases a large difference in mobility between the two components exists: the WISE spectrum, which provides in F_2 dimension informations about the chemical structure by ^{13}C chemical shift, and in F_1 dimension data about the molecular mobility by the proton wide line spectrum, can evidence mobility difference for different components [19]. Our materials, in which PS and PB are at room temperature well below and above their T_gs, respectively, and a relevant amount of interfacial matter is supposed to be present, appear particularly suitable for this approach.

In the aliphatic region of ^{13}C spectrum (0–60 ppm referred to tetramethylsilane scale) at about 40 ppm the signal of PS chain ($-CH-$ and $-CH_2$ groups) is observable and at 32 and 27 ppm the signals of trans- and cis-methylene groups of PB, respectively, are evident. In general the proton spectrum for PS shows a very broad line, with a width of several tens of kHz, while the equivalent for PB exhibits a sharp line with a width of some kHz*. On the other hand, if we analyse the WISE spectra of the considered HIPS materials we can see for all samples along F_1 dimension a broadening at the base of PB signals, and a sharp line superimposed on the PS signal clearly indicating the presence of a mixing phase with an intermediate mobility.

Fig. 18 shows the spectra for A30 and B20: the comparison is sound because the two materials have approximately the same chemical composition (PB amount is 6.1% and 6.3% for A30 and B20, respectively, as computed from the polymerisation composition data and confirmed from ordinary infrared spectroscopy and iodometric measurements). From the figure it is evident that the shapes of PB signals are clearly different in the two materials: B20 signals are higher than A30. Taking in account that PB content is the same and then the

---

*The proton NMR line is wide in solids because of the strong dipolar couplings, while it sharpens in liquids because the coupling mechanism is less efficient.

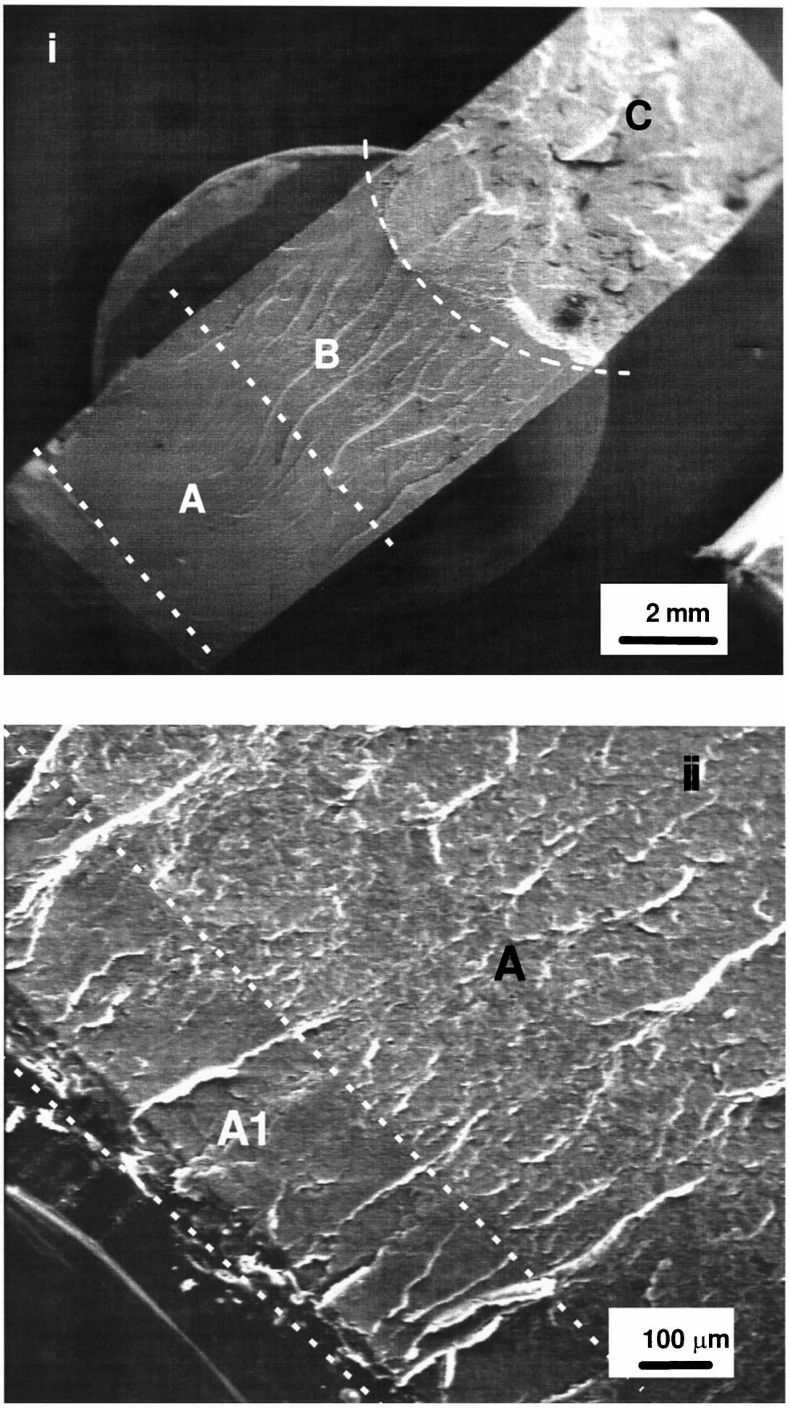

Figure 22 SEM overview of a SCF surface in material B5. The picture above (i) shows that there are different fracture zones: (A) Very slow propagation: $da/dt < 10^{-5}$ m/s, (B) stable propagation: 10^{-5}m/s $< da/dt < 10^{-3}$ m/s, (C) catastrophic propagation: $da/dt > 10^{-3}$ m/s. The picture below (ii) evidences that the zone (A) has a narrow sub-zone (A1), relative to the very start of the fracture.

volume of the peaks must also be the same, this shape variation indicates that B20 signals are less broad at the base than A30, which means that the *mixing* between PS and PB is worse in B20 than in A30. In order to make this conclusion stronger it is also possible to compare spectra in constant second phase conditions: Fig. 19 displays A20 and B20 spectra. In this case the difference between the two materials is analogue and even enhanced.

Despite the fact that the NMR information regards the molecular mobility and it is difficult to transform it in terms of quantity of interfacial matter and/or of molecular weight and structure of the graft copolymer, it is definitely possible to say that the NMR confirms the hypothesis that the PS-PB interface has in B *deficient characteristics* with respect to its counterpart in material A, causing the debonding of particles under the action of thermal and/or mechanical stress.

Coming now to the poor capability of B particles in stopping the crazes, we notice that the observation that B particles are poor in PS sub-inclusions is useful also here. When we consider craze arrest on a rubbery particle we use a language not exactly correct. In general, in fact, the craze is not properly arrested: it tends to propagate *through* the particle originating some *intra-particle fibrillation* (Fig. 20). Probably it is during this

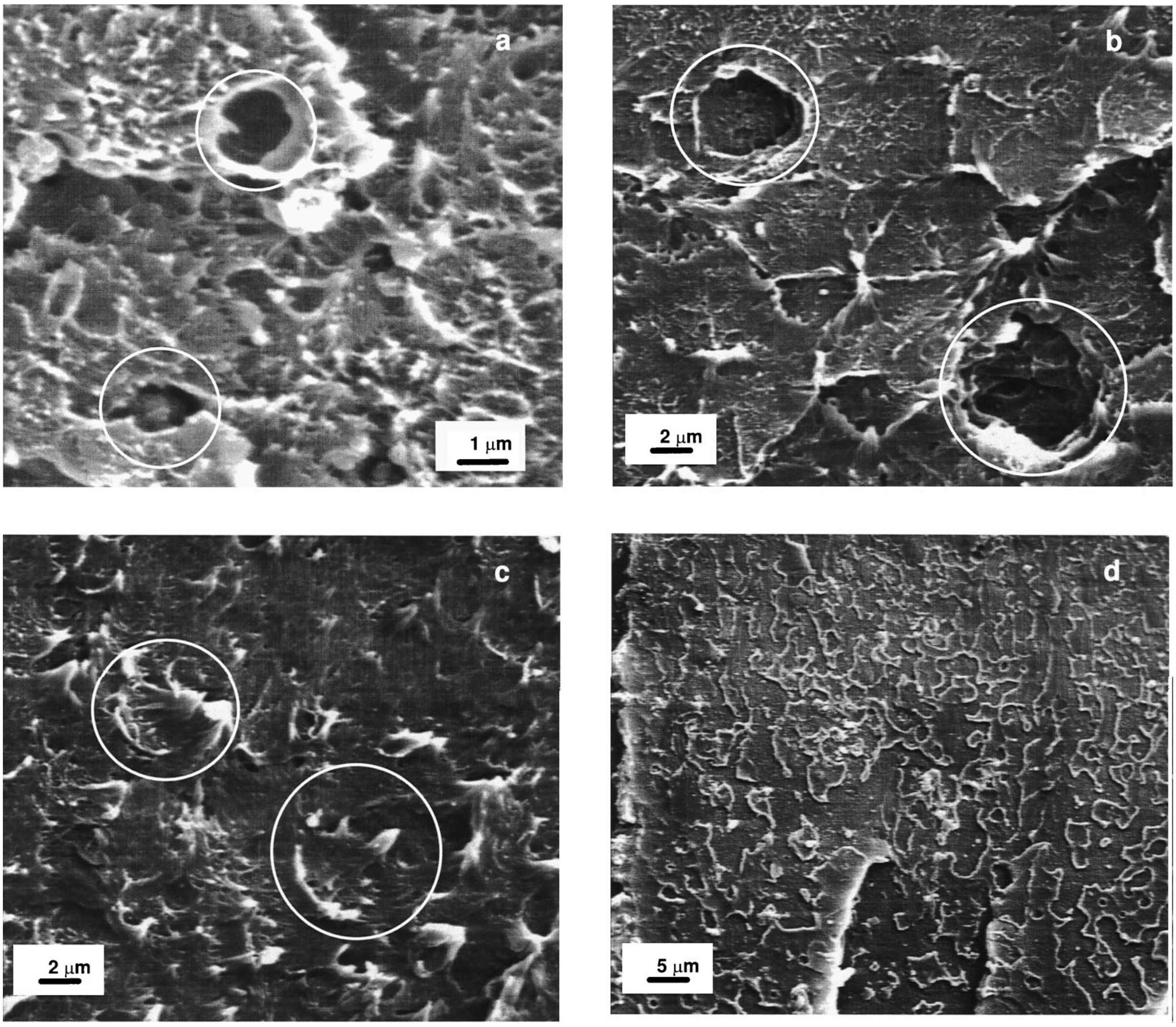

Figure 23 SEM micrographs of a SCF surface in material B5: (a) zone A1, (b) zone A, (c) zone B, (d) zone C. Particle debonding is evident in zones A1 and A (white circles). In zones B and C no debonding is evident (white circles indicate adherent particles). The zones are those indicated in Fig. 22.

intra-particle fibrillation, because of the stress relaxation of the rubber, that the crazes looses its driving force. If this intra-particle relaxation mechanism is inhibited due to an high PS content, like in B, the particle does not represent an obstacle to the craze propagation and can fracture as well.

If these ideas can explain well the brittle SCF behaviour of B, we have now to understand why, when impact fracture is concerned the same material does not show remarkable differences with respect to A. Unfortunately the TEM *in situ* deformation cannot be performed at high speed: we do not have then a direct evidence of the fracture micromechanisms during impact tests. Nonetheless the SEM investigation of the fracture surfaces is extremely useful in this case. When fracture surfaces from both SCF and Impact experiments are observed for material A, one finds that the rubbery particles always appear adherent to the matrix and broken on the crack path (Fig. 21). The situation, on the contrary, is much more complicated for material B. The SCF surface for material B5 presents several different zones, corresponding to different crack speeds (Figs 22 and 23): it is possible to observe that in the zones corresponding to very slow crack speeds the fracture surface is characterised by holes which coincide to debonded and pulled particles, while the phenomenon is much less relevant at higher speed (Fig. 23) and almost absent in impact fracture surfaces, where, on the contrary, broken, adherent particles similar to those observed for A are visible (Fig. 24). Holes and debonded particles in SCF surfaces are less frequent when the second phase volume fraction is increased.

These evidences, while it substantially confirms the debonding phenomenon (seen in TEM pictures and evidenced in dynamic mechanical measurements for B materials) and straightens the hypothesis of a thermal stress contribution, due to the massive holes presence in low ϕ samples, offers also the possibility to understand the fracture behaviour difference when different strain rates are involved. In fact we have to assume that the particle-matrix debonding for material B is governed by some chain pull-out of the grafted molecules at the interface. We know then that this phenomenon is greatly dependent on the pull-out rate, and then on the crack velocity: experimental and theoretical studies have demonstrated indeed that the fracture toughness of an interface greatly increases with increasing the crack speed [29–35]. In the material B, then, a considerable number of particle-matrix interfaces can fail, besides those already opened by thermal stresses, when the

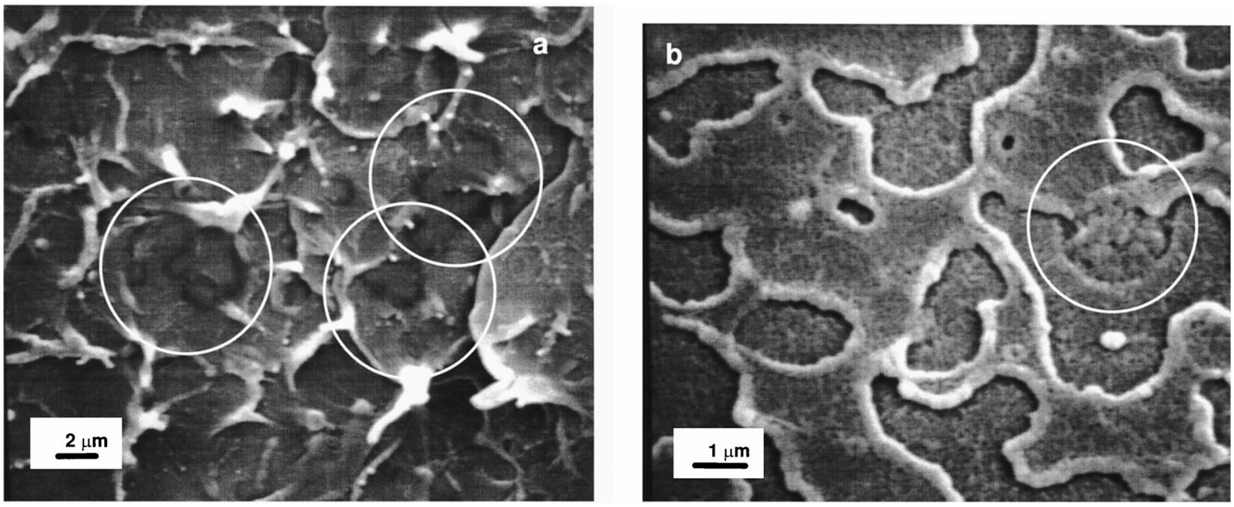

Figure 24 SEM micrographs of an impact fracture surface in material B5. The surface has two distinct zone: a first one (a) quite ductile, and a second one (b) more brittle. In both zones bonded, broken particles are visible (white circles).

crack speed is slow, as in SCF experiments, while they will probably resist in high crack speed conditions. The debonding phenomenon, which is obviously a dramatic source of damage and detrimental to the fracture performance, will be possibly absent in impact fracture conditions, giving to material B a performance very similar to A.

The SCF behaviour of HIPS puts then in evidence structural characteristics, like the particle-matrix adhesion, which rarely affect the standard mechanical measurements (elastic properties, impact toughness). Thus the analysis of HIPS only in pure morphological terms (second phase volume fraction and size), which is quite simple and consolidated, could in principle not be sufficient in order to completely predict the mechanical behaviour in service.

4. Conclusions

The main conclusion of the present paper is that SCF and impact fractures can exhibit very different features: for instance the SCF behaviour in HIPS evidences that the particle-matrix interfacial features, which in general do not affect ordinary mechanical tests (elastic properties, impact toughness, etc.), can play instead a relevant role in slow fractures. In this case in fact some chain pull-out at the interface can cause particle debonding and premature fracture as a consequence.

Furthermore, from the investigation here presented, we consider promising the development of the NMR to explore interfacial properties in real multiphase polymeric materials, of which we presented an example.

Acknowledgements

The authors thank G. Romagnoli and L. Monti (EniChem) for providing materials, P. Corradini, C. Zanni and M. Vighi (EniChem) for their collaboration in doing experiments and P. Lomellini, L. Monti, G. P. Ravanetti (EniChem), C. Fond (C. Sadron, Strasbourg) and C. Créton (ESPCI, Paris) for their helpful comments. The electron microscopy investigation involving the straining holder device has been done by CM at the Institut Interdepartemental de Microscopie Electronique of the Ecole Polytechnique Fédérale de Lausanne, whose staff is gratefully acknowledged for their kind support.

References

1. C. MAESTRINI, A. CALLAIOLI, M. ROSSI and R. BERTANI, *J. Mater. Sci.* **32** (1996) 3747.
2. P. C. PARIS and F. ERDOGAN, *Trans. ASME* **85** (1963) 528.
3. P. C. PARIS, in Proceedings 10th Sagamore Conference, Syracuse, New York, 1964.
4. A. McEVILY and R.C. BOETTNER, *Acta Metall* **11** (1963) 725.
5. G. R. IRWIN and J.A. KRIES, *Weld. J. Res. Suppl.* **33** (1951) 1935.
6. G. R. IRWIN, *Appl. Mat. Res.* **3** (1964) 65.
7. C. B. BUCKNALL, "Toughened Plastics" (Applied Science Publishers, London, 1977).
8. E. J. KRAMER, *Adv. Polym. Sci.* **52/53** (1983) 1.
9. E. J. KRAMER and L. L. BERGER, *ibid.* **91/92** (1990) 1.
10. C. MAESTRINI, M. MERLOTTI, M. VIGHI and E. MALAGUTI , *J. Mater. Sci.* **27** (1992) 5994.
11. C. MAESTRINI, K. PISONI and H. H. KAUSCH, *ibid.* **31** (1996) 3249 .
12. G. GIACONI, L. CASTELLANI, C. MAESTRINI and T. RICCÒ, *Polymer* **39** (1998) 6315.
13. K. KATO, *Polym. Eng. Sci.* **7** (1967) 38.
14. J. G. WILLIAMS, "Fracture Mechanics of Polymers" (Ellis Horwood, Chichester, 1984).
15. D. P. ROOKE and D. J. CARTWRIGHT, "Compendium of Stress Intensity Factors" (Ministry of Defense, London, 1974).
16. J. G. WILLIAMS and M. W. BIRCH, "Fracture 1977" (ICF4, Canada, 1977).
17. T. VU-KHANH, *Polymer* **29** (1988) 1979.
18. B. D. LAUTERWASSER and E. J. KRAMER, *Phil. Mag.* **A39** (1979).
19. K. SCHMIDT-ROHR, J. CLAUSS and H.W. SPIESS, *Macromolecules* **25** (1992) 3273.
20. J. N. GOODIER, *J. Appl. Mech.* **55** (1933) 39.
21. C. MAESTRINI, L. MONTI. and H. H. KAUSCH, *Polymer* **37** (1996) 1607.
22. O. ISHAI and L. COHEN, *J. Compos. Mater.* **2** (1968) 302.
23. C. MAESTRINI, L. CASTELLANI, M. MERLOTTI and M. VIGHI, *Polymer* **33** (1992) 1556.
24. L. MORBITZER, D. KRANZ, G. HUMME and K. H. OT, *J. Appl. Polym. Sci.* **20** (1976) 2691.
25. A. PAVAN and T. RICCÒ, *J. Mat. Sci. Lett.* **11** (1976) 1180.

26. C. CRETON, H. R. BROWN and K. R. SHULL, *Macromolecules* **27** (1994) 3174.
27. M. DERUELLE, L. LÉGER and M. TIRELL, *ibid.* **28** (1995) 7419.
28. W. Z. CAI, K. SCHMIDT-ROHR, N. EGGER, B. GERHARZ and H. W. SPIESS, *Polymer* **34** (1993) 267.
29. A. N. GENT and A. J. KINLOCH. *J. Polym. Sci. A2* **49** (1971) 659.
30. A. N. GENT and J. SCHULTZ, *J. Adhesion* **3** (1972) 281.
31. E. H. ANDREWS and A. J. KINLOCH, *Proc. R. Soc. London A* **332** (1973) 385.
32. *Idem., ibid.* **332** (1973) 385.
33. H. BROWN, *Macromolecules* **23** (1993) 1666.
34. E. RAPHAEL and P. G. DeGENNES, *J. Phys. Cem.* **96** (1992) 4002.
35. M. RUBINSTEIN, A. AJDARI, L LEIBLER, F. BROCHARD-WYART and P. G. DeGENNES, *C. R. Acad. Sci. (Paris) Ser II* **316** (1993) 317.

Received 1 September 1998
and accepted 21 June 1999